

Stretchable Shape-Sensing Sheets

Dylan Shah, Stephanie J. Woodman, Lina Sanchez-Botero, Shanliangzi Liu, and Rebecca Kramer-Bottiglio*

Soft robot deformations are typically estimated using strain sensors to infer change from a nominal shape while taking a robot-specific mechanical model into account. This approach performs poorly during buckling and when material properties change with time, and is untenable for shape-changing robots that don't have a well-defined resting (unactuated) shape. Herein, these limitations are overcome using stretchable shape sensing (S3) sheets that fuse orientation measurements to estimate 3D surface contours without making assumptions about the underlying robot geometry or material properties. The S3 sheets can estimate the shape of target objects to an accuracy of ≈ 3 mm for an 80 mm long sheet. The authors show the S3 sheets estimating their shape while being deformed in 3D space and also attached to the surface of a silicone three-chamber pneumatic bladder, highlighting the potential for shape-sensing sheets to be applied, removed, and reapplied to soft robots for shape estimation. Finally, the S3 sheets detecting their own stretch up to 30% strain is demonstrated. The approach introduced herein provides a generalized method for measuring the shape of objects without making strong assumptions about the objects, thus achieving a modular, mechanics model-free approach to proprioception for wearable electronics and soft robotics.

1. Introduction

Sensing our body's shape is crucial for many, if not all, of our daily activities. When our proprioceptive feedback systems malfunction, the consequences can be dire, ranging from decreased joint stability^[1] to bodily damage including possible osteoarthritis.^[2] In robotics, proprioception is equally as fundamental, playing an essential role in executing safe, controlled motions.


Numerous approaches to proprioception in robots have been proposed. Rigid-link robots can estimate their shape accurately by measuring the angles between the links, and applying forward

kinematics^[3] and accompanying dynamics.^[4–7] However, an emerging class of robots comprises continuously deformable segments, rendering the rigid-body assumption invalid. Many approaches to soft robot state estimation pair a model with several strain sensors, exploiting the fact that much of the surface area and interior volume of soft robots stretch during use. For example, researchers have proposed numerous schemes for sensor-based closed-loop control of continuum robots,^[8] including for medical applications.^[9] Another particularly well-studied class of soft robots is soft grippers, where many methods were used to sense shape,^[10–12] including a few demonstrations of closed-loop control of soft grippers.^[13,14] The strain sensors used include resistive sensors made of liquid metal (eutectic gallium-indium, or EGaIn)^[10,11] or conductive polymer composites,^[12] and multilayer capacitive sensors using conductive polymer composites.^[15–17] Despite these promising advances, strain sensor-based

methods have some inherent limitations. For example, Case et al. showed how several common silicones can change mechanical properties over time and even when deformed at different rates, making modeling challenging.^[18] Additionally, it is unclear how to generalize these advances in strain-based shape estimation to reconfigurable soft robots^[16,19–21] or robots whose resting shape changes during their lifetime.^[22,23] In both reconfigurable and shape-changing robots, the resting shape dramatically changes, violating the basic assumptions utilized in strain-based techniques, such as the constant-curvature or piecewise-constant-curvature models in widespread use with manipulators.^[8]

In a step toward decoupling shape estimation from the modeling and design of the robot, researchers have proposed numerous sensorized surfaces. Several authors have proposed using flexible fabric or plastic sheets to connect several rigid, sensorized elements, and then estimating the relative orientation between sections with known geometries (using, e.g., an inertial measurement unit, or IMU), to determine the spatial locations of discrete points within a sheet.^[24–27] In a related but different approach, Huard and Sprynski et al. proposed a continuously deformable, sensorized sheet to measure 3D space curves.^[28,29] Other approaches to surface estimation use machine learning and statistics to process sensor data and extract a continuous estimate of the shape of the target surface.^[30–32] For instance, Rendl et al. used 16 piezoelectric

D. Shah, S. J. Woodman, L. Sanchez-Botero, S. Liu, R. Kramer-Bottiglio
School of Engineering & Applied Science
Yale University
New Haven, CT 06520, USA
E-mail: rebecca.kramer@yale.edu

 The ORCID identification number(s) for the author(s) of this article can be found under <https://doi.org/10.1002/aisy.202300343>.

© 2023 The Authors. Advanced Intelligent Systems published by Wiley-VCH GmbH. This is an open access article under the terms of the Creative Commons Attribution License, which permits use, distribution and reproduction in any medium, provided the original work is properly cited.

DOI: 10.1002/aisy.202300343

bend sensors on a polyethylene terephthalate (PET) sheet to approximate the shape of the sheet as a combination of several shape primitives.^[30] Meerbeek et al. embedded an array of optical fibers in an elastomeric foam, and used machine learning algorithms to identify the mode of deformation and estimate the angle of deformation of the foam.^[32] One drawback of the data-driven approaches^[30–32] is that it is unclear how the algorithms would generalize to shapes not seen during training. Furthermore, these prior sensorized surfaces (both the data-driven and rigid-link approaches) could not stretch, making them incompatible with many soft robots.

In this study, we introduce stretchable shape-sensing (S3) sheets (Figure 1). The sheets comprise acrylic adhesive, biphasic gallium indium alloy (bGaIn) circuits,^[33] and commercial integrated circuits (ICs) that provide orientation and strain measurements. We demonstrate S3 sheets reconstructing their shape in free space and on several static shapes with known geometry, achieving an estimation accuracy of ≈ 3 mm on an 80 mm sheet. We also show the sheets applied to the surface of a three-chamber pneumatic bladder, highlighting their ability to estimate dynamic shape change of arbitrarily shaped soft robots, without knowledge of the robot's geometry or material properties. Finally, we characterize the stretch sensor response while straining the sheets to 30%. Overall, the S3 sheets can be applied to an arbitrary host body to estimate its shape and changes in shape, then removed and applied to a different host to do the same, cumulatively achieving a modular and mechanics model-free approach to proprioception.

2. Results

2.1. Circuit Overview

We made S3 sheets using sensorized stretchable circuit board assemblies and used an offboard PC to postprocess the sensor

data for shape estimation (Figure 1). To manufacture the sheets, we painted conductive traces of bGaIn^[33] on both sides of a stretchable double-sided acrylic tape (0.5 mm-thick VHB 4910, 3M Inc.), and then placed commercial surface-mount electrical components on the circuits, including absolute orientation sensors (BNO055, Bosch), capacitive sensing ICs (MPR121, Arrow Semiconductor), resistors, and capacitors. To measure the stretch along the S3 sheets, we painted bGaIn traces on the top in a rectangular strain-gauge rosette centered around each MPR121 (Figure 2a), and painted ground traces on the bottom layer directly underneath these electrodes, to form capacitive stretch sensors.^[15,17,34] To reduce the effects of cross-talk (intracircuit electromagnetic interference), we included bypass capacitors on the supply lines and aligned the ground planes of the interintegrated circuit (I2C) communication lines with their positive rails. External noise did not cause issues in our experiments, but in noisier environments, it may be necessary to protect signal integrity by including ground pours on the top and/or bottom of the circuit. Further manufacturing details are presented in the Experimental Section.

The orientation and stretch sensing modalities fulfill complementary roles. The absolute orientation sensors provide a relatively low-noise estimate of the surface normal at discrete points, while also providing orthogonal vectors in the tangent plane. Further, absolute orientations reduce the propagation of error from sensors earlier in the serial chain, when compared to relative orientations reported by an IMU. The BNO sensors' three vectors specify a unique coordinate system at each location, helping to remove orientational uncertainties that can arise from approaches relying solely on stretch sensors or relative orientation sensors, but they do not provide any explicit information about the distance between points on the surface. Meanwhile, the stretch sensor rosettes give information about the sheets' 2D strain state, a feature that will be useful in future sheets that

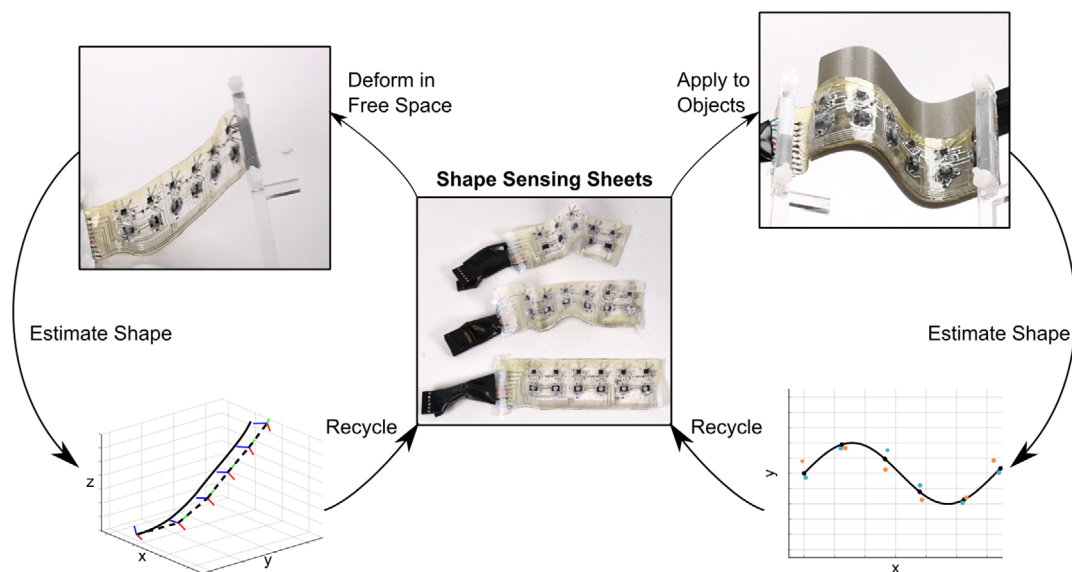


Figure 1. Stretchable shape-sensing (S3) sheets can stretch and bend to measure the shape of complex surfaces. The S3 sheets (middle) can estimate their shape while they are deformed in 3D space (left) or applied to objects (right), without requiring additional modeling or sensor fusion algorithms to deal with each different application or use case. Each sheet has a nominal unstretched length of 80 mm.

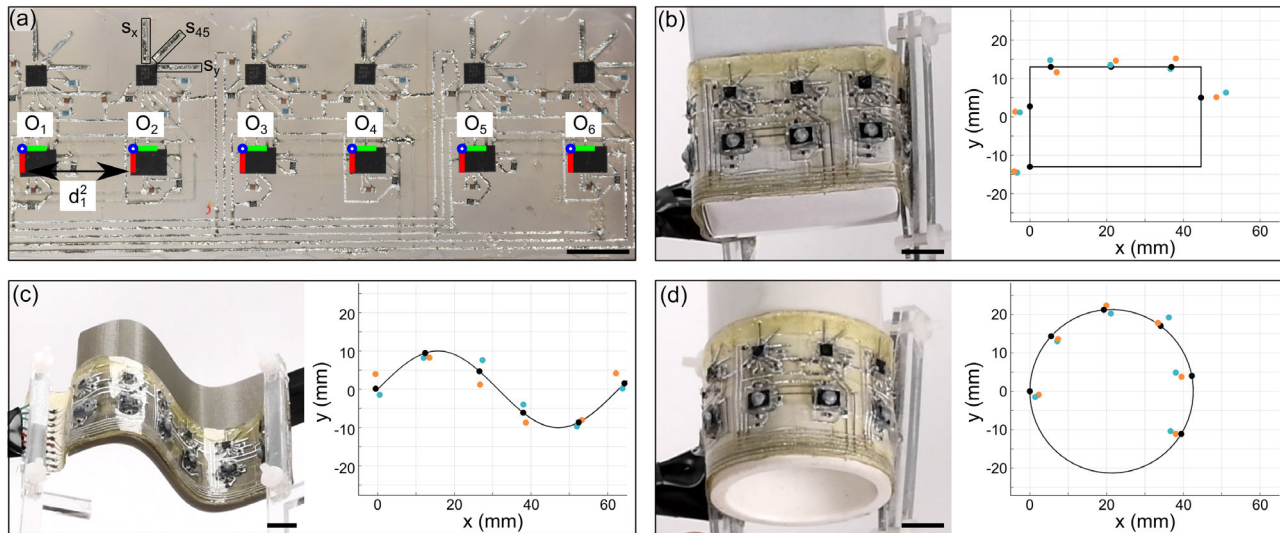


Figure 2. Using S3 sheets to estimate the surface profiles of several objects. a) Coordinate systems and geometry for the S3 sheets. The positions P_i of the origin of each coordinate system O_i are our primary values of interest. Additionally, we have used black boxes to indicate three strain sensors within a single module. Note that O_0 and O_1 are coincident, but differ by a rotation R_0^1 . Red lines show x axes, green lines show y axes, and blue circles indicate that the z axes point out of the page (toward the camera in this view). b–d) Representative results for shape estimation of known geometries. Black dots show ground truth, gold dots show the rigid-link approximation, and blue dots show the slerp estimation. (b) A rectangular prism with dimensions 44.6×26 mm. (c) A sinusoid with equation $y = 10 \sin(x/10)$. (d) A cylinder with diameter 42.6 mm. Scale bars, 1 cm.

are firmly embedded in biaxially stretchable surfaces, such as shape-changing robots.^[35]

2.2. Shape-Estimation Algorithms

During use, the S3 sheet will be deformed into a shape, the sensors give data, and we must find algorithms to minimize the error between the estimated shape and the true shape. Different interpolation methods and shape-estimation algorithms may perform better under specific sets of motions. For clarity and generality, we will focus on two fusion algorithms: a rigid-link assumption and approximating the sheets as a smooth curve using spherical interpolation of tangent vectors with discrete integration.

First, we must become more precise in our notion of shape and error. Numerous methods exist to quantify differences in shape, after minimizing rotation, scaling, and translation errors,^[35,36] including the elastic deformation energy required to stretch and bend one shape into another without cutting or puncturing it,^[37] heuristics such as the “shape index” ($S = \frac{\text{Perimeter}}{2\sqrt{\pi \cdot \text{area}}}$),^[38] and the sum of squared differences between important landmark points along the two surfaces in Procrustes analysis.^[39,40] Here, we are interested in quantifying the shape of a discretely sensorized stretchable sheet at an instant in time, and we can easily apply Procrustes analysis for evaluating our sheets and comparing performance to other (nonstretchable) shape-sensing sheets.

Starting with a base coordinate system O_0 , defined at the corner of the leftmost orientation sensor (with gravity pointing in the negative z direction), we can define a series of coordinate systems of interest O_i ($i = 1, 2, \dots, 6$) that are located at the corner

of each of our orientation sensors, with the z axis oriented normal to their surface (Figure 2a). The 3D position of these origins will be denoted as P_i , defined in the base coordinate system O_0 unless specified otherwise. This coordinate system notation is analogous to the traditional Denavit–Hartenberg notation^[3] used in traditional robotics. However, in traditional robots, the local “joint frames” correspond to the robot’s degrees of freedom. In the case of an S3 sheet, there are infinite degrees of freedom, and potentially infinite interesting local frames to use. To minimize confusion while retaining all available information, we have included precisely one joint frame per orientation sensor. The straight-line distances between them will be defined as d_i^{i+1} , while the distance between neighboring coordinate systems, along the surface of the skin, will be defined as l_i^{i+1} .

To estimate the shape of a series of rigid links connected by spherical joints (i.e., they can rotate about arbitrary axes), one simply needs to determine the coordinate transforms between the bases of each link. We will apply this simplified model to our S3 sheet, in what we will call the rigid-link assumption. Specifically, we define the y -axis of O_i (denoted as y_i) to point toward P_{i+1} , and we define the distance between P_i and P_{i+1} to be d_i^{i+1} . Thus

$$P_{i+1} = P_i + d_i^{i+1} * y_i \quad (1)$$

Note that the orientation sensors used (Bosch BNO055) are global orientation sensors, allowing each sensor to be truly independent and preventing error propagation as the sensor count increases. This is in contrast to a typical orientation sensor, such as an inertial measurement unit (IMU), which would only give relative rotations. We can collect the coordinate frame axes for each sensor into a single rotation matrix R_i , and express the transformation T_i , in O_0 coordinates, as

$$P_{i+1} = P_i + d_i^{i+1} * R_i * [0, 1, 0, 1]' = P_i + T_i^{i+1} * [0, 0, 0, 1]' \quad (2)$$

where we have expanded the homogeneous coordinates for an origin point, to make it explicit that we are expressing the location of an origin. We can then express each coordinate as $P_i = [0, 0, 0, 1 - i] + \sum_{j=0}^{i-1} T_j^{i+1} [0, 0, 0, 1]'$, where the first term $[0, 0, 0, 1 - i]$ is introduced to ensure that the point is still expressed in homogeneous form. This first term is the main modification required relative to the traditional Denavit–Hartenberg parameters,^[3] wherein the use of relative orientation sensors allows progressive homogeneous transforms to be multiplied together to make a new homogeneous transform.

If there is negligible stretch in the system, as in the case of a freely moving sheet, then the distances l_i^{i+1} are all constant. Additionally, for relatively small curvatures, $d_i^{i+1} \approx l_i^{i+1}$, allowing the skin to operate entirely using the orientation sensors. For increased accuracy, by premultiplying the initial (flat, unstretched) lengths $l_{i_0} = d_{i_0}$ with their stretch factor γ_i (obtained from the stretch sensors), we can get an estimate of the current length $l_i^{i+1} = \gamma_i * l_{i_0} \approx d_i^{i+1}$. However, to fully estimate the curved shape of the skin between the successive orientation sensors, we need to introduce other nonlinear connecting arcs.

To demonstrate how smoothly-varying curves can be used for interpolation instead of a rigid-link model, we use an approach inspired by the work of Saguin–Sprynski et al.^[27] Specifically, with tangent vectors given by the sensors as γ_i and γ_{i+1} , we first interpolate with spherical interpolation (shorthanded as “slerp”) to get a smooth estimate t_s of the tangent curves connecting the points, with known arc-lengths

$$t_s(\gamma_i, \gamma_{i+1}, s) = \frac{\sin((1-s)\theta)\gamma_i + \sin(s\theta)\gamma_{i+1}}{\sin(\theta)} \quad (3)$$

where θ is the angle between γ_i and γ_{i+1} , and the arc-length parameter $s \in [0, 1]$ allows us to get an arc-length parameterization of the tangent vectors along the unit sphere. This guarantees the tangent vectors will be unit length, while including the constraint that the tangents match the tangents of the orientation sensors. Note that, in the limit when $\theta = 0$, this yields the classical linear interpolation. Finally, we can numerically integrate the tangent estimates with constant step size l_i/n with n subdivisions of s (such that the total arc length is identically l_i^{i+1}) to get smooth estimates of the curves connecting our orientation sensors, as desired

$$P_{i+1} = P_i + \sum_{j=0}^n l_i^{i+1} / n * t_s(\gamma_i, \gamma_{i+1}, j/n) \quad (4)$$

2.3. Surface Contour Estimation of 3D Objects

By applying the S3 sheets to the surface of objects, we can estimate the objects’ surface profiles. The sheets can stretch and bend to fill the contours of the surface, allowing their orientation sensors to get accurate readings of the surface normals. Here, we explore this possibility by applying the sheets to objects with known ground-truth shapes to estimate their surface contour.

By studying these base shapes, we can begin to quantify the strengths and limitations of the current hardware, pointing to future opportunities and challenges.

Applying the sheets to a variety of geometrically distinct objects allows us to estimate their surface contours (Figure 2). Here, we conformed a sheet to the surface of a rectangular prism (Figure 2b), sinusoid (Figure 2c), and a cylinder (Figure 2d). These shapes represent a complexly curved surface, a discrete polygon, and a constant-curvature surface, respectively, highlighting the generality of the approach. For each shape, we recorded 5 s of data at 30 Hz for five independent S3 sheet applications. After each application, the skin was laid flat on a table, then reapplied to the shape for an independent measurement. The total error, including intrinsic sensor noise and errors due to reapplication of the sheet (representing the envisioned use case of reconfigurable S3 sheets), yielded a root-mean-square error (RMSE) of 3.5, 3.6, and 2.0 mm for the rectangular prism, sinusoid, and cylinder, respectively, using the rigid-link model. Using the slerp smooth interpolation, we achieved an RMSE of 3.04, 2.7, and 1.5 mm, respectively, suggesting that smooth interpolation is a better estimator than the rigid-link approximation. Finally, we note that the “null algorithm” of assuming the sheet was flat would yield much higher RMSEs of 7.11, 12.3, and 15.3 mm, respectively.

Note that the accuracy of these curves, in particular discrete shapes like the rectangular prism, is dependent on where the six origins are placed: the skin has no knowledge of where discontinuities may lie on the surface. Hence, the change in orientation between two origins could be due to an infinite number of curves between the two origins. However, most objects are concave and do not have large, irregularly shaped protrusions, so the error is often small. The Nyquist–Shannon sampling theorem tells us that the S3 sheets can only accurately measure variations in shapes that have a wavelength (or characteristic length) that is more than double the spacing between orientation sensors. Increasing the sensor density—and therefore, the number of origins of interest—can allow for the estimation of more complex surface profiles. However, current semiconductor packaging technologies limit the sensing ICs (accelerometers, capacitive sensing chips, etc.) to a minimum size of approximately 3 by 3 mm, introducing a tradeoff between sensor density and the deformability of the circuit. Additionally, the offset between the target shape and the orientation sensors represents a fixed offset error and a slight smoothing function, making it desirable to manufacture the sheets to be as thin as possible. Here, we used 0.5 mm VHB (sold as 0.02 inches thick), making substantial further improvements in this regard unlikely.

2.4. Estimation of 3D Space Curves

To test the limits of the S3 sheets under simultaneous bending and torsion, we deformed the sheets using rigid bars, and estimated the sheets’ shape using both the rigid-link method (for ease of visualization) and the more-accurate spline method (Figure 3). While the shape-estimation appears accurate, the dense sensor spacing and occlusions during motion made it difficult to obtain ground truth for the sheets’ shape. A complete

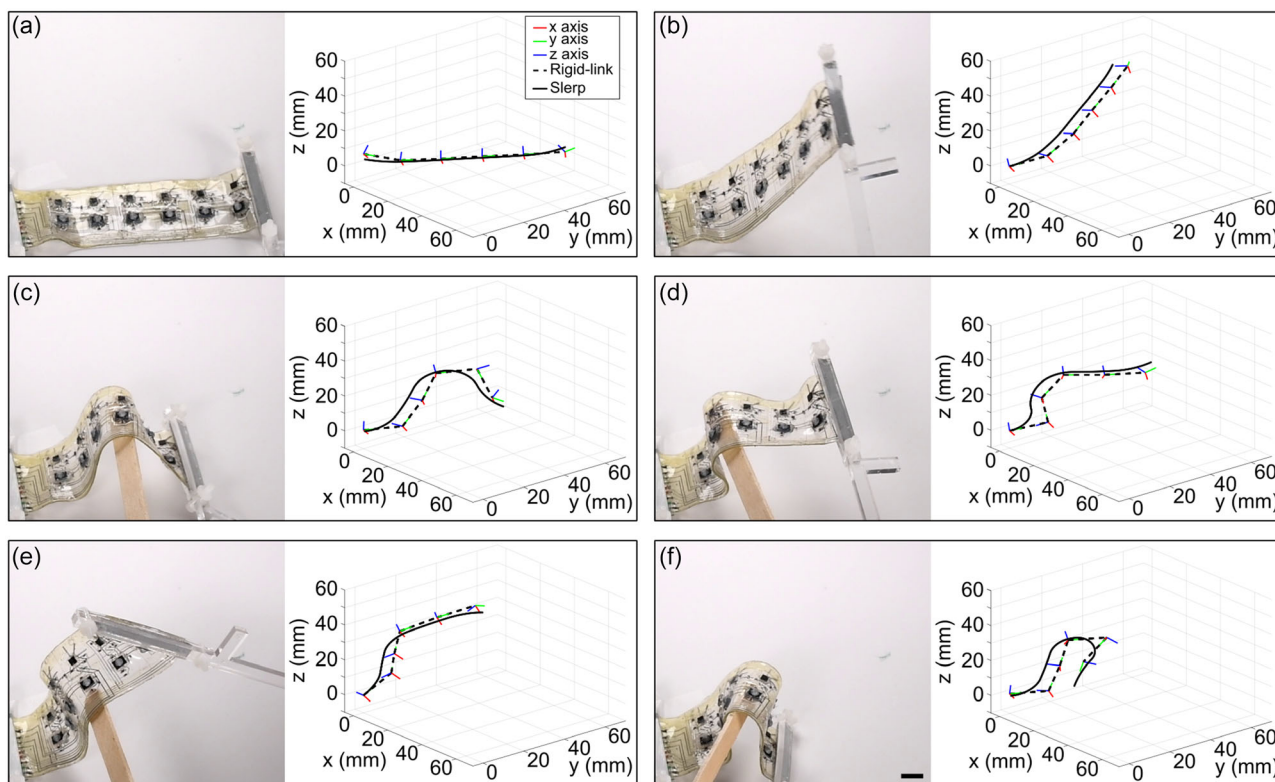


Figure 3. Shape estimation of 3D space curves. Left, photos of the skin deformed in various shapes. Right, estimated shape using the rigid-link approximation as well as the slerp interpolation, alongside the coordinate frame of each orientation sensor. a) Flat. b) Curved upward. c) Lifted in the middle, making a concave downward shape. d) Bent around a wooden stick into a step-like curve. e) Bent and twisted simultaneously. f) Lifted in the middle and tucked in a highly contorted “Ω” shape. Scale bar in (f) is 1 cm, and applies to all images.

video of the dynamic estimation of the sequence of motions shown in Figure 3 can be found as Movie S1, Supporting Information.

Moving sequentially through the subfigures, we have attempted curves with increasing variations in curvature. Initially, we can see that the orientation of the first sensor, O_1 is tilted downward slightly due to the grips lifting the sheet off of the flat surface (Figure 3a). However, the remaining sensors are all aligned well, highlighting the global nature of the orientation sensors. The curve was then lifted into a smooth curve with a visually accurate sensor reconstruction (Figure 3b). With the introduction of a rigid stick, two inflection points were added to the curve, making it more difficult for the sheets to estimate their shape with the rigid-link assumption and increasing the value of utilizing spline-based methods such as slerp (Figure 3c,d). Next, we see how the orientation sensors naturally detect torsion (Figure 3d), in contrast to stretch or bend sensors, which can estimate at most a single degree of freedom and require additional sensors to distinguish between curvature and torsion. Finally, as the curvature increases into a highly-curved “Ω” shape, the rigid-link assumption results in physically unrealistic cusp nodes, while slerp approximates the curve but misses some of the nuances due to the characteristic length of the bend being of the same order of magnitude as the sensor spacing (Nyquist–Shannon sampling theorem).

Since S3 sheets can estimate arbitrary 3D space curves, they can also be applied to the surface of soft robots to measure their motion. To illustrate this concept, we applied an S3 sheet to the surface of a three-chamber pneumatic bladder (Figure 4 and Movie S2, Supporting Information). The estimated shape starts flat with the bladders (including the O_1 sloped-down error as noted previously), then as the bladders are inflated, the skin detects the motion and adjusts its estimation to be curved with the bladders’ overall shape. Since the sheets could not detect their overall height, we have set the lowest estimated point at $z = 0$. Using this baseline, the sheets successfully estimated the shape and orientation of the surface, highlighting the generality of the previous 3D space curves estimation.

2.5. Stretchability

The S3 sheets can also detect their stretch, using the capacitive sensors emanating from the MPR121 ICs. Each MPR121 is connected to three sensors arranged in a rectangular rosette configuration, which, in theory, can detect the full 2D strain state. However, we had difficulty getting all MPR121s working simultaneously, thus we include this feature as a proof-of-concept, and have not utilized the stretch functionality for our shape-estimation experiments. To highlight the stretchability of the circuits, we stretched an S3 sheet along

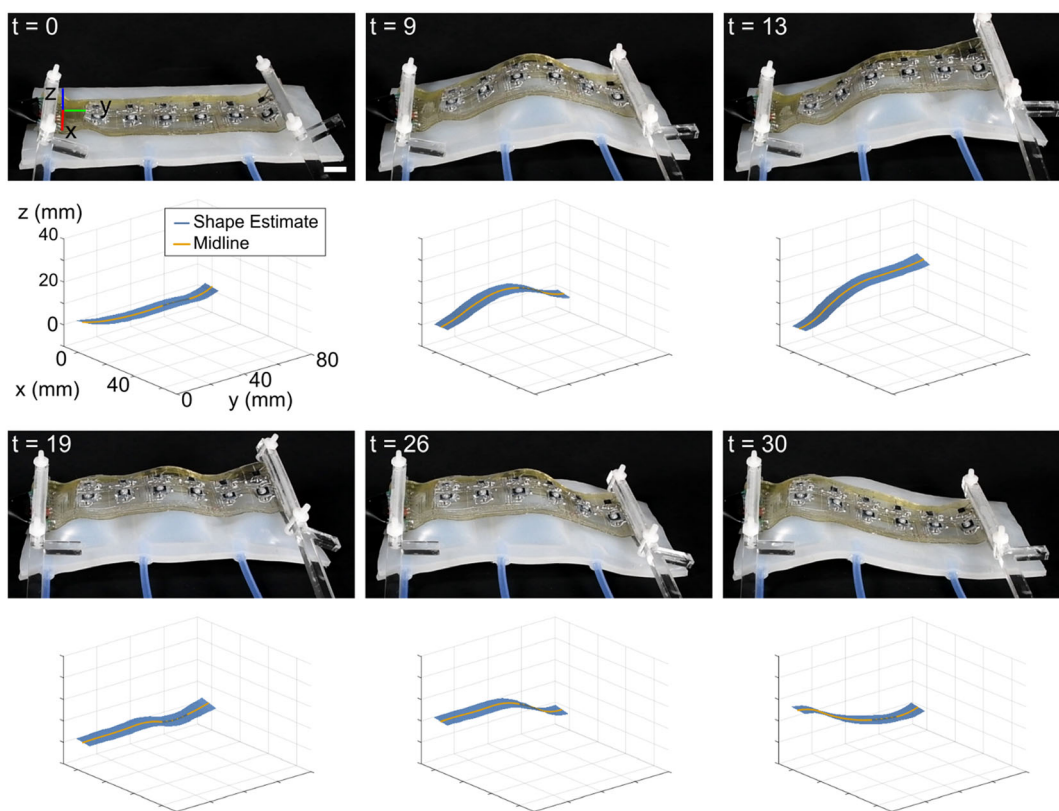


Figure 4. Using S3 sheets to estimate surface profiles of a multichamber pneumatic bladder. The plots below each photo show the estimated shape of the surface of the bladder. Since the sheets have no concept of elevation, we have defined the lowest point of the skin to be $z = 0$. From top-left to bottom-right: flat, middle bladder inflated, middle and right bladders inflated, all bladders inflated, left and middle bladders inflated, and left bladder inflated. The scale bar in $t = 0$ denotes 1 cm, and applies to all images.

the y direction to 30% strain ($\epsilon = 0.3$) cyclically, and plotted the sensor data from a complete module (Figure 5, with photos of a stretched circuit presented in Supporting Information).

Due to their small size (6 mm long, 0.75 mm wide), the sensors have a relatively low capacitance, on the order of 10 pF (Figure 5). While each sensor has a different starting capacitance (likely due to variations in the trace width), the change in capacitance correlates linearly with stretch in the ideal case.^[17,41]

In practice, viscoelastic effects and the sensors' nonzero width coupled with the Poisson effect lead to imperfect sensor behavior, complicating estimation of the 2D strain state with the stretch sensor rosettes. Despite these challenges, after the initial slack region of ≈ 0 –8% strain, the response of each sensor attached to a given MPR121 is distinct: the sensors aligned with the stretch direction (s_y and t_y) exhibited the largest response ($\approx 0.12 \mu\text{F}$), while the sensors at 45° exhibited a smaller response,

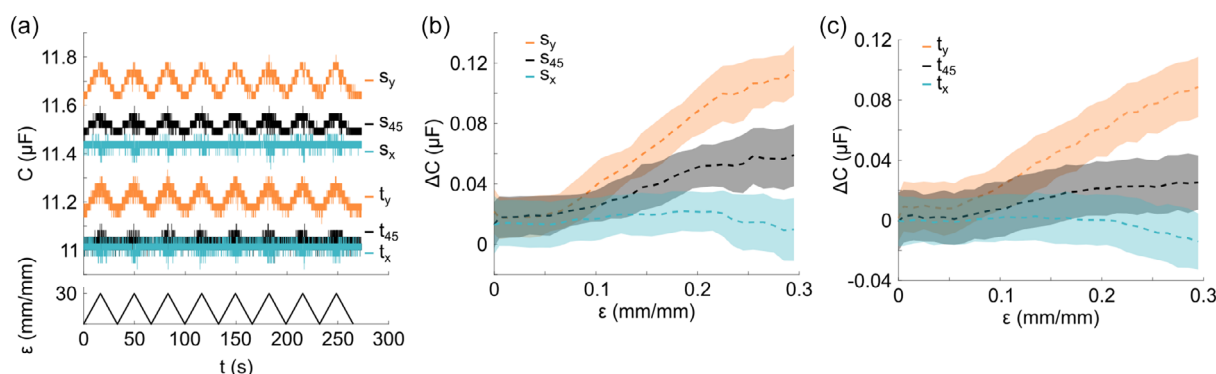


Figure 5. Stretchability of the shape-sensing sheets. Here, we stretched the sheets along the y direction to 30% eight times. a) Raw sensor data from two MPR121 IC's, with three stretch sensors each (oriented aligned with the x axis, angled at 45° , and aligned with the y axis). b,c) Change in capacitance versus stretch, for two sets of strain sensors s_i and t_i . Dashed lines denote the mean, while clouds indicate 1 standard deviation from the mean.

and the sensors aligned with the x axis exhibited a slightly negative response. This negative response could be due to the shortening of the sensors (contraction due to Poisson's ratio, lowering capacitance) overpowering the effect of the sensor getting wider (elongation in the y direction, increasing capacitance).

In this study, we found that small interfaces were the most challenging, with the quad flat no-lead (QFN) packages used here (pin width 0.2 mm and pin spacing 0.4 mm) beginning to fail at roughly $\epsilon = 30\%$. To investigate whether corrosion was a likely cause (since EGaIn is corrosive on many metals), we conducted scanning electron microscope/energy dispersive X-ray spectroscopy (SEM-EDS) analysis on MPR121 chips in three conditions: a pristine (unused) state; after being used in an S3 sheet circuit; after being used in an S3 sheet and cleaned (see the , Supporting Information). We observed no noticeable change in composition of the electrodes after being cleaned, suggesting that the EGaIn was not corroding or otherwise alloying with the electrode surfaces, which were primarily nickel and palladium.

3. Conclusion

In this manuscript, we introduced flexible and stretchable sheets that can estimate their shape. This represents an advance toward the estimation of surface profiles of soft robots, which could be used to execute high-DoF closed-loop shape change. The removable sheets do not make assumptions about the underlying substrate, making it straightforward to apply, remove, and reapply the S3 sheets to the surface of soft robots with differing morphologies.

Limitations of the present S3 sheets could be overcome through synergistic advances in stretchable circuits, material interfacing, and shape reconstruction algorithms. At strains over 30%, the ICs begin to lose connection and discontinue functioning. Potential routes to improve the IC interfacing include the use of copper strain islands,^[42] and the use of HCl vapor to improve bonding with the liquid metal traces.^[43] The use of an automated pick-and-place machine could reduce component alignment errors, and the use of purely elastic materials (without viscoelastic effects) could prolong the S3 sheets' lifespan by reducing unwanted wrinkling. Increasing the sensor density could yield higher-resolution estimates of shape. To apply the S3 sheets to larger surfaces, a multitude of sheets could be connected in a gridlike arrangement, and sensor fusion algorithms, such as those proposed by Stanko et al.,^[44] could be used to combine the information from each S3 sheet and estimate the shape of large stretchable surfaces. We are currently working toward utilizing such a grid to measure the shape of shape-changing robots^[35] as they morph during locomotion, stretching in multiple directions. Finally, future advances in stretchable computing could allow the S3 sheets to execute shape-estimation onboard in real time.

Collectively, this work points to a new approach to shape-sensing for soft robotics and wearables. Roboticists could fuse orientation and strain information to get estimates of curves and surfaces on their robots without requiring extensive system modeling and mechanical characterization. This allows two major design challenges to be decoupled—robot design can be done more independently of the sensing design, then general-purpose S3 sheets can be attached to the robots' surfaces.

4. Experimental Section

Manufacturing: To manufacture the sheets, we made traces on double-sided acrylic tape (VHB 4910) using biphasic gallium-indium (bGaIn),^[33] encapsulated using rubber cement (Elmer's Products, Inc.) and mechanically placed commercial ICs (Figure 6). Specifically, we first attached wax-coated paper (the backing of XFasten carpet tape) to VHB, and laser-cut the outline and vias with a CO₂ laser (ULS 3.0, Universal Laser Systems) (Step 1). Then, we used an ultraviolet laser (LPKF U4) to cut circuit outlines into the sticker paper on the top and bottom (Step 2). Next, we prepared an EGaIn suspension by adding EGaIn (1.8 g) to ethanol (11 mL), followed by sonication using a probe sonicator (Qsonica, Q700) coupled with a 1/4 inch diameter microtip (part number 4420) at 30% amplitude for 2 h. To induce oxide formation and create bGaIn, the suspension was poured into a crucible and baked in an oven (Lindberg Blue M, Thermo Fisher Scientific) at 900° for 30 min. We then painted bGaIn on the bottom of the VHB, removed the bottom sticker paper, and encapsulated the traces with rubber cement (Steps 3–4). After flipping the circuits over, we painted bGaIn on the other ("top") side (Step 5). This completed the substrate preparation.

To transform the traces into functional circuits, we then placed components with a 3-axis manual pick-and-place machine (custom made using an Edmund Optics camera-positioning system, Step 6). Next, wires were added using silicone adhesive (SilPoxy, Smooth-On, Inc.), and the border was encapsulated with rubber cement (Steps 7–8). Leaving the ICs exposed during this step made it easier to debug and repair circuits when they stopped working. Finally, we added SilPoxy on the border of each IC to reduce shear strain at their interfaces with bGaIn (Step 9).

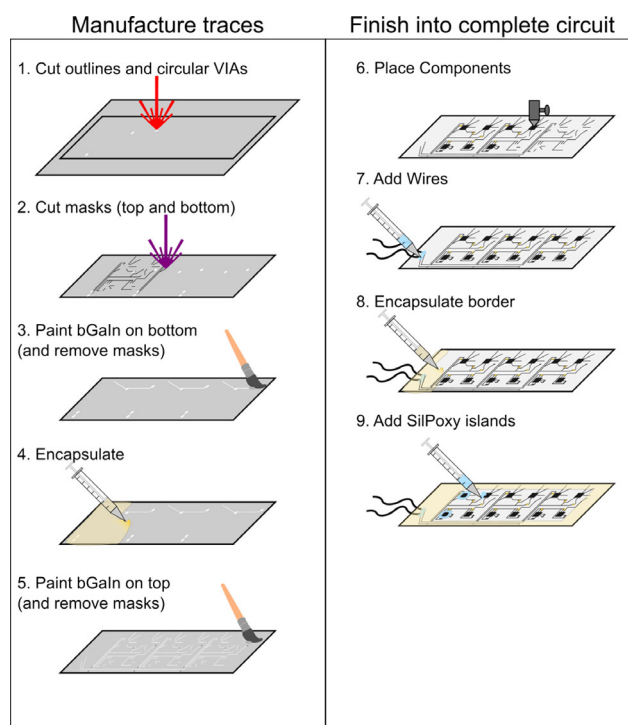


Figure 6. Manufacturing an S3 sheet. First, the traces were manufactured using VHB, sticker paper masks, and rubber cement to encapsulate the bGaIn traces. Then, we added electrical components (ICs, resistors, capacitors) and wires, encapsulated the border, added SilPoxy islands around each IC, and attached motion-capture markers onto the orientation sensors to serve as ground truth.

Supporting Information

Supporting Information is available from the Wiley Online Library or from the author.

Acknowledgements

This work was supported by the National Science Foundation (NSF) under grant no. EFMA-1830870. D.S.S. was supported by a NASA Space Technology Research Fellowship (grant no. 80NSSC17K0164). S.J.W. was supported by a NASA NSTGRO Fellowship (grant no. 80NSSC22K1188). L.S.B. was supported by NSF grant no. IIS-1954591.

Conflict of Interest

The authors declare no conflict of interest.

Author Contributions

D.S.S. and R.K.B. conceived the project, planned the experiments, and managed the research. D.S.S., L.S.B., S.W., and S.L. designed and built the hardware. D.S.S. wrote the algorithms. D.S.S. and S.J.W. performed the experiments. All authors drafted and edited the manuscript. All authors contributed to, and agree with, the content of the final version of the manuscript.

Data Availability Statement

The data that support the findings of this study are available from the corresponding author upon reasonable request.

Keywords

reconfigurable robots, robotic skins, soft robotics, stretchable electronics

Received: June 20, 2023

Revised: August 24, 2023

Published online:

- [1] B. L. Riemann, S. M. Lephart, *J. Athl. Train.* **2002**, *37*, 80.
- [2] L. Sharma, Y.-C. Pai, *Curr. Opin. Rheumatol.* **1997**, *9*, 253.
- [3] J. Denavit, *ASME J. Appl. Mech.* **1955**, *77*, 215.
- [4] F. Flacco, T. Kröger, A. D. Luca, O. Khatib, in *2012 IEEE Int. Conf. Robotics and Automation*, IEEE, Piscataway, NJ **2012**, pp. 338–345.
- [5] A. D. Luca, F. Flacco, in *2012 4th IEEE RAS EMBS Int. Conf. Biomedical Robotics and Biomechatronics (BioRob)*, IEEE, Piscataway, NJ **2012**, pp. 288–295.
- [6] O. Khatib, *Int. J. Rob. Res.* **1986**, *5*, 90.
- [7] A. Spröwitz, A. Tuleu, M. Vespignani, M. Ajalloeian, E. Badri, A. J. Ijspeert, *Int. J. Rob. Res.* **2013**, *32*, 932.
- [8] T. George Thuruthel, Y. Ansari, E. Falotico, C. Laschi, *Soft Rob.* **2018**, *5*, 149.
- [9] J. Burgner-Kahrs, D. C. Rucker, H. Choset, *IEEE Trans. Rob.* **2015**, *31*, 1261.
- [10] J. Tapia, E. Knoop, M. Mutný, M. A. Otaduy, M. Bächer, *Soft Rob.* **2019**, *7*, 332.
- [11] R. A. Bilodeau, E. L. White, R. K. Kramer, in *2015 IEEE/RSJ Int. Conf. Intelligent Robots and Systems (IROS)*, IEEE, Piscataway, NJ **2015**, pp. 2324–2329.
- [12] T. G. Thuruthel, B. Shih, C. Laschi, M. T. Tolley, *Sci. Rob.* **2019**, *4*, eaav1488.
- [13] J. Morrow, H. Shin, C. Phillips-Grafflin, S. Jang, J. Torrey, R. Larkins, S. Dang, Y. Park, D. Berenson, in *2016 IEEE Int. Conf. Robotics and Automation (ICRA)*, IEEE, Piscataway, NJ **2016**, pp. 5024–5031.
- [14] G. Gerboni, A. Diodato, G. Ciuti, M. Cianchetti, A. Menciassi, *IEEE/ASME Trans. Mechatron.* **2017**, *22*, 1881.
- [15] E. L. White, M. C. Yuen, J. C. Case, R. K. Kramer, *Adv. Mater. Technol.* **2017**, *2*, 1700072.
- [16] J. W. Booth, D. Shah, J. C. Case, E. L. White, M. C. Yuen, O. Cyr-Choiniere, R. Kramer-Bottiglio, *Sci. Rob.* **2018**, *3*, eaat1853.
- [17] A. Tairy, I. A. Anderson, *Soft Rob.* **2019**, *6*, 389.
- [18] J. C. Case, E. L. White, R. K. Kramer, *Soft Rob.* **2015**, *2*, 80.
- [19] S. Y. Kim, R. Baines, J. Booth, N. Vasios, K. Bertoldi, R. Kramer-Bottiglio, *Nat. Commun.* **2019**, *10*, 3464.
- [20] J. Zhang, A. Jackson, N. Mentzer, R. Kramer, *Front. Rob. AI* **2017**, *4*, 46.
- [21] J. Zou, Y. Lin, C. Ji, H. Yang, *Soft Rob.* **2018**, *5*, 164.
- [22] D. S. Shah, J. P. Powers, L. G. Tilton, S. Kriegman, J. Bongard, R. Kramer-Bottiglio, *Nat. Mach. Intell.* **2021**, *3*, 51.
- [23] S. Kriegman, S. Walker, D. Shah, M. Levin, R. Kramer-Bottiglio, J. Bongard, in *Robotics: Science and Systems XV*, Freiburg im Breisgau, Germany **2019**, <https://www.roboticsproceedings.org/rss15/p28.pdf>.
- [24] T. Hoshi, H. Shinoda, in *2008 SICE Annual Conf.*, Chofu, Japan **2008**, pp. 915–920, <https://doi.org/10.1109/SICE.2008.4654785>.
- [25] P. Mittendorfer, G. Cheng, in *2012 IEEE/RSJ Int. Conf. Intelligent Robots and Systems*, IEEE, Piscataway, NJ **2012**, pp. 4505–4510, <https://doi.org/10.1109/IROS.2012.6385559>.
- [26] A. Hermanis, R. Cacurs, M. Greitans, *IEEE Sens. J.* **2016**, *16*, 1271.
- [27] N. Saguin-Sprynski, L. Jouanet, B. Lacolle, L. Biard, in *EWSHM - 7th European Workshop on Structural Health Monitoring*, Nantes, France **2014**, pp. 702–709, <https://hal.inria.fr/hal-01020418>.
- [28] M. Huard, N. Sprynski, N. Szafran, L. Biard, *Numerical Algorithms* **2013**, *63*, 483.
- [29] M. Huard, R. T. Farouki, N. Sprynski, L. Biard, *Graphical Models* **2014**, *76*, 30.
- [30] C. Rendl, D. Kim, S. Fanello, P. Parzer, C. Rhemann, J. Taylor, M. Zirkl, G. Scheipl, T. Rothländer, M. Haller, S. Izadi, in *Proc. 27th Annual ACM Symp. User Interface Software and Technology, UIST '14*, ACM, New York, NY **2014**, pp. 129–138, <https://doi.org/10.1145/2642918.2647405>.
- [31] T. L. T. Lun, K. Wang, J. D. L. Ho, K. Lee, K. Y. Sze, K. Kwok, *IEEE Rob. Autom. Lett.* **2019**, *4*, 1454.
- [32] I. M. V. Meerbeek, C. M. D. Sa, R. F. Shepherd, *Sci. Rob.* **2018**, *3*, eaau2489.
- [33] S. Liu, D. S. Shah, R. Kramer-Bottiglio, *Nat. Mater.* **2021**, *20*, 851.
- [34] B. O'Brien, T. Gisby, I. A. Anderson, *Proc. SPIE* **2014**, *9056*, 905618.
- [35] D. Shah, B. Yang, S. Kriegman, M. Levin, J. Bongard, R. Kramer-Bottiglio, *Adv. Mater.* **2020**, *33*, 2002882.
- [36] A. A. Taha, A. Hanbury, *BMC Med. Imaging* **2015**, *15*, 29.
- [37] K. Patrice, H. Joel, *J. R. Soc. Interface* **2015**, *12*, 0150795.
- [38] I. Slavkov, D. Carrillo-Zapata, N. Carranza, X. Diego, F. Jansson, J. Kaandorp, S. Hauer, J. Sharpe, *Sci. Rob.* **2018**, *3*, 25.
- [39] K. S. Arun, T. S. Huang, S. D. Blostein, *IEEE Trans. Pattern Anal. Mach. Intell.* **1987**, *PAMI-9*, 698.
- [40] P. H. Schönemann, *Psychometrika* **1966**, *31*, 1.
- [41] E. L. White, J. C. Case, R. Kramer-Bottiglio, *Soft Rob.* **2018**, *5*, 36.
- [42] D. G. Marques, P. A. Lopes, A. T. D. Almeida, C. Majidi, M. Tavakoli, *Lab Chip* **2019**, *19*, 897.
- [43] K. B. Ozutemiz, J. Wissman, O. B. Ozdoganlar, C. Majidi, *Adv. Mater. Interfaces* **2018**, *5*, 1701596.
- [44] T. Stanko, S. Hahmann, G.-P. Bonneau, N. Saguin-Sprynski, *Comput. Graphics* **2017**, *66*, 74.